Geophysical Research Letters

Supporting Information for

Pitted Terrains on (1) Ceres and Implications for Shallow Subsurface Volatile Distribution

H. G. Sizemore*[1], T. Platz[2], N. Schorghofer[1], T. H. Prettyman[1], M. C. De Sanctis[4], D. A. Crown[1], N. Schmedemann[5], A. Neesemann[5], T. Kneissl[5], S. Marchi[6], P. M. Schenk[7], M. T. Bland[8], B. E. Schmidt[9], K. H. G. Hughson[10], F. Tosi[4], F. Zambon[4], S. C. Mest[1], R. A. Yingst[1], D. A. Williams[11], C. T. Russell[10], C. A. Raymond[12]

[1]Planetary Science Institute, Tucson AZ, USA,
[2]Max Planck Institute for Solar System Research, Göttingen, Germany,
[4]Istituto di Astrofisica e Planetologia Spaziali, INAF, Rome, Italy,
[5]Freie Universität Berlin, Berlin, Germany,
[6]Southwest Research Institute, Boulder, CO, USA,
[7]Lunar and Planetary Institute, Houston, TX, USA,
[8]USGS Astrogeology Science Center, Flagstaff, AZ, USA
[19]Georgia Institute of Technology, Atlanta, GA, USA,
[10]University of California Los Angeles, Los Angeles, CA, USA,
[11]Arizona State University, Tempe, AZ, USA,
[12]Jet Propulsion Laboratory, California Institute of Technology, Pasadena, CA, USA.

Contents of this file (part 1)

Text S1 to S12
Figures S1 to S5
Table S1

Contents of 2nd file (part 2)

Figures S6 to S12

Introduction

The supplementary materials include context and detailed images of cerean all cerean craters in which pits have been identified (S1-7), as well as technical background for pit size measurements (S8), sublimation (S9) and outgassing (S11) calculations, comparisons to extra-cerean morphological features (S10), and a description of thermal image analysis (S12).

Text S1-S7: Overview of Pit-Hosting Craters

Figs. S1-S7 show context images of Ikapati, Haulani, Dantu, Kupalo, Urvara, Occator, and Azacca craters and details of their associated pitted terrains. See discussion in the manuscript and in figure captions.

Text S8: Pit Size Measurements and Crater Size Relationships

We analyzed global mosaics and individual FC LAMO images to map the approximate extent of pitted terrains and to quantify the diameter and depth of individual large pits. Reddy et al. [2012] described the FC data pipeline and mosaicking techniques in detail. We identified individual pits for measurement using global clear filter LAMO mosaics in equidistant cylindrical projection with ArcGIS software. At each crater where pits were identified, we measured the diameter of the 10-20 largest pits using the CraterTools add-in for ArcGIS [Kneissl et al., 2011]. This method has the advantage of producing accurate measurements independent of map projection. Most pits were sufficiently circular to allow for good fits based on three points defined at the pit margins. Fig. S8 shows pit diameter as a function of crater diameter, a power law fit the to the cerean data, and power law fits to martian data by Tornabene et al. [2012].

We quantified the depth of individual pits using two methods. We derived relative elevation profiles of the largest pits in Ikapati and Dantu from stereo pairs of LAMO images using ISIS image processing software [Fig. 2 in main text; Becker et al., 2015]. Elsewhere (Haulani, Urvara, Azacca), we approximated the depth of individual large pits by measuring shadow lengths. Due to low image resolution, we considered depths based on shadow length to be order-of-magnitude estimates only.

Text S9: Sublimation Timescales

We used a numerical model of sublimation and diffusion to quantify the gradual loss of water ice from a regolith-ice matrix to space, based on temperature and the physical properties of the near-surface materials. We evaluated two scenarios. In the first, the initial ice fraction equals the porosity of the ice-free material of 40%. In the second, the initial ice content is 90% by volume, and a sublimation lag with 40% porosity remains

after the ice has receded; due to the excess ice content, this lag is thinner than the depth over which the ice table has receded.

The model applied to the first scenario (40% ice by volume) is described in detail in Schorghofer [2016]. Calculations are asynchronously coupled in the sense that thermal cycles are evaluated 100 times every solar day (a time step of ~5.4 minutes) over 20 orbits, and the sublimation rate from the last of these orbits is used to advance the ice table, which retreats at a much slower pace, over many millions of years. The thermal cycle is periodically re-calculated to take into account the changing thermal properties and the increase in solar luminosity. In the current study, total integration time is 1 Ga, greater than the total lifetime of the oldest craters in which pits were identified.

The model applied to the second scenario (90% ice by volume) differs from the first only by the collapse of the sublimation lag. When the volumetric ice fraction ψ is larger than the porosity ν of the ice-free material, the thickness of the lag z_T grows at a rate of

$$\frac{dz_T}{dt} = \frac{\beta}{\rho_{ice}} D \frac{\rho_{sv}}{z_T} \tag{S1}$$

with the geometric factor

$$\beta = \frac{1-\psi}{1-\nu}\frac{1}{\psi} \tag{S2}$$

where $D(\nu)$ is the vapor diffusivity and ρ_{sv} is the saturation vapor pressure averaged over the last orbit. Upon integration this leads to the time-stepping scheme

$$z_T^{(n+1)} = \sqrt{z_T^{(n)2} + 2D\beta\rho_{sv}\Delta t/\rho_{ice}} \quad \text{for} \quad \psi \geq \nu \tag{S3}$$

The model calculations assume a thermal inertia for the ice-free material of 15 $\mathrm{Jm^{-2}K^{-1}s^{-1/2}}$, based on earth-based observations [Rivkin et al. 2010], whereas the ice-rich layer has a much higher thermal inertia. The particle size in the surface layer must be small to be consistent with the low thermal inertia, and is assumed to be 10μm, which sets the scale for the mean-free-path of diffusing water molecules. There is some unavoidable arbitrariness in the assumptions about the physical properties of the regolith, but the rate of sublimation loss is mainly governed by temperature, which primarily

depends on distance from the sun, latitude, and the thermal inertia of the surface layer [e.g., Schorghofer, 2008].

A suite of model calculations has been carried out for various latitudes. Model results are shown in Fig. S9.

Text S10: Mecurian "Hollows" and Martian "Swiss Cheese" Terrain

Martian, vestan and cerean pitted materials are morphologically distinct from landforms produced by sublimation on Mars and other bodies, indicating a different formation mechanism. Fig. S10 shows examples of terrains attributed to sublimation on Mercury and Mars to emphasize this distinction. Mercurian "hollows" (Fig. S10A-C) are flat-floored, commonly have high-reflectance interiors and halos, and exhibit highly complex margins that give their host terrain an etched appearance (i.e. individual pits are elongate and sometimes branching). Blewitt et al. [2011] attributed this morphology to sublimation as well as possible space weathering of a shallow volatile layer based on the high albedo of hollow interiors and halos and strong morphological similarities to the martian south polar Swiss Cheese Terrain [Malin et al. 2001; Fig. S10D-F], which has been firmly linked to sublimation of CO_2 [Byrne and Ingersoll, 2003]. In contrast to both mercurian hollows and martian Swiss Cheese terrain, the pits discussed in this manuscript exhibit highly irregular floor depths, and circular-to-irregular margins. Although we identified individual pits and depressions with elliptical-to-irregular boundaries on Ceres – i.e. pits that were slightly elongated -- nowhere did we observe pits with highly elongated, complex, branching margins. Further, cerean pits and pitted terrains are not distinct from the their surroundings in terms of albedo or color; host materials range from very bright (i.e. at Haulani) to very dark (i.e. the Urvara floor).

Text S11: Application of the Boyce et al. [2012] Pit Production Model to Ceres

We calculated gas pressures, flow velocities, and the maximum size of silicate clasts elutriated by gas flow for Ceres following the development outlined in Appendix A of Boyce et al. [2012]. In this treatment, gas pressure in the pore space of a melt-bearing layer is assumed to equal or exceed the overburden pressure at the base of the layer to drive pit-forming flows. For laminar flow, the pressure as a function of depth is given by:

$$P^2 = P_o^2 - \left[\frac{8F_v\eta_g QT_a}{vmr^2}\right] z^2, \quad \text{(S4)}$$

where P is the pressure at depth z, P_o is the pressure at the layer base, Q is the universal gas constant, T_a is the temperature of the melt bearing layer and the escaping steam, v is the porosity or void space fraction, η_g is the gas viscosity, and m is the molecular mass of H_2O. F_v is the steam generation rate for laminar flow:

$$F_v = \frac{(P_o^2 - P_a^2)}{z_o^2}\frac{vmr^2}{8\eta_g QT_a}, \quad \text{(S5)}$$

where P_a is pressure at the planetary surface (0 Pa at Ceres). In the case of turbulent flow, the steam production rate is

$$F_v = \frac{(P_o^2 - P_a^2)}{z_o^3}\frac{3v^2mr}{2fQT_a}, \quad \text{(S6)}$$

where f is a friction factor for gas flow past particles in tube walls, and the pressure is given by

$$P^2 = P_o^2 - \left[\frac{2F_v fQT_a}{3v^2mr}\right] z^3. \quad \text{(S7)}$$

In both the laminar and turbulent cases the gas velocity reduces to

$$U_g = \left[\frac{F_v QT_a}{P_v m}\right] z. \quad \text{(S8)}$$

The pressure and velocity profiles are calculated for both flow regimes, and the regime that produces the lower velocities is considered to be physically relevant.

The radius, r_{max}, of the largest spherical clast that can resist being elutriated by gas flowing at speed U_g is found by equating the upward drag force on the clast to the clast's weight:

$$r_{max} = \left[\frac{3\rho_g C_D U_g^2}{8\rho_r g}\right], \quad \text{(S9)}$$

where C_D is a drag coefficient dependent on clast shape but of order unity.

We considered an initial layer thickness of 100 m to allow direct comparison to results reported by Boyce et al. [2012] for Mars. Fig. S11 shows the results of these calculations. Table S1 shows a comparison of parameter values assumed for Mars [Boyce et al., 2012] and Ceres (this study). We found that flow velocities on Ceres are generally comparable to flow velocities predicted for Mars, although this result is sensitive to the assumed porosity in the melt-bearing layer and to the temperature of the silicate material. The reduced acceleration due to gravity and the low density of silicate materials on Ceres

relative to Mars both result in a lower pressure requirement to drive flow and the entrainment of larger clasts at a given velocity when flow is established.

As noted above, we assumed that gas pressure in the pore space of the melt-bearing layer must equal or exceed the overburden pressure at the base of the layer to drive pit-forming flows. The overburden pressure at the base of a 100 m layer of impact material is 4.7e4 Pa on Ceres, assuming a CI grain density of 2.1 g/cc and 20% porosity. Applying the ideal gas law and assuming a temperature of 500 K in a melt-bearing layer [Marchi et al. 2013], this corresponds to ~0.1% of the water that could be liberated from $MgSO_4$ $6H_2O$ with a 1 wt.% concentration in an otherwise anhydrous porous silicate layer. Similarly, 4.7e4 Pa is roughly 0.01% of the water that could be liberated from ice filling the pore space of the brecciated layer. Based on gas velocities predicted by the Boyce et al. [2012] mode, we estimated the H_2O production rate during pit development at Ikapati at ~2e32 molecules/s, assuming conservatively that pit throats comprise 1% of the area mapped as pitted terrain in this region (Fig. 2 in main text).

Text S12: Thermal Imaging of Pitted Terrains

On Vesta pitted terrains in young craters are associated with thermal anomalies in VIR data [Denevi et al., 2012; Tosi et al., 2014; Capria et al., 2014]. We searched for thermal anomalies associated with cerean pitted terrains in VIR data obtained during HAMO using techniques established at Vesta [Tosi et al., 2014]. In contrast to Vesta, pitted terrains on Ceres are *not* associated with apparent thermal anomalies. Fig. S6 shows a comparison of visible and thermal imaging data at Dantu; results at Ikapati and Haulani are similar.

At the spatial scale of VIR observations in HAMO (~370-380 m/px), there are no obvious thermal signatures associated with pits in Haulani, Dantu, and Ikapati, implying that there is no substantial variation in thermal conductivity and/or density of the surface material at lengthscales of several hundred metres. Haulani, Dantu, Ikapati and Kupalo were observed at higher resolution by VIR in LAMO, but observation conditions are not optimal for this analysis (non-contiguous footprints, smearing, and high phase angles all contributed to low overall SNR). For comparison, the pitted terrain in the floor of crater Marcia on Vesta showed a thermal contrast at a spatial resolution of ~700 m/px, which

became more apparent in subsequent, higher-resolution images (~200 m/px).

Thermal differences at Vesta and Ceres may reflect both compositional and grain-size variation between the regoliths of the two bodies. In some regions of Mars, young/fresh craters are recognized based on the presence of "thermal" rayed craters in nighttime thermal images from the Mars Odyssey (MO) Thermal Emission Imaging System (THEMIS). However, pristine craters containing pits – e.g., Tooting Crater – are also recognized on morphological grounds without a thermal signature. The martian pitted materials were first recognized and documented in both Tooting Crater and the thermal rayed craters [Mouginis-Mark and Gabriel, 2007; Malin and Edgett, 2001; Tornabene et al., 2006; Preblich et al., 2007]. Martian craters with pits are now recognized globally on terrains with thermal inertias ranging from 46 to 486 SI units [Tornabene et al., 2012].

Table S1: Parameter comparison for flow velocity calculations relevant to Mars and Ceres.

Parameter	Units	Mars (Boyce et al.)	Ceres (this study)
Porosity, v		0.125	0.1, 0.15, 0.2
Layer depth, z_o	m	100	100
Clast density, ρ_r	kg m^{-3}	2500	2200
Gravitational acc., g	m s^{-1}	3.73	0.2789
Overburden pressure, p_o	Pa	0.74e6	5.3e4, 5.0e4, 4.7e4
Vapor viscosity, η_g	Pa s	6.0e-5	6.0e-5
Temperature, T	K	1023	300, 500
Surface pressure, P_a	Pa	700	0
Grain radius, r_p	m	11.3e-3	11.3e-3
Friction factor for turbulent flow, f		0.03	0.03

Annex 1

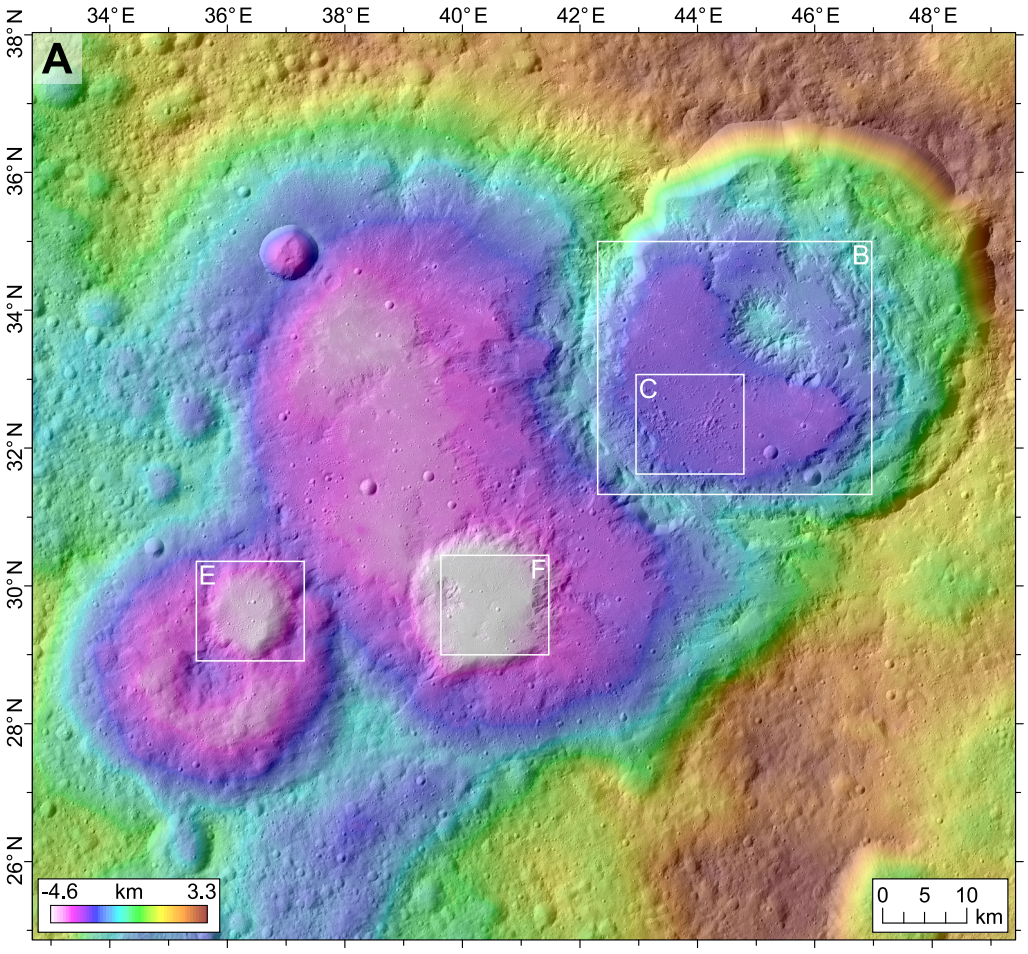
A
B
C
E
F
-4.6 km 3.3
0 5 10 km
34° E
36° E
38° E
40° E
42° E
44° E
46° E
48° N
36° N
34° N
32° N
30° N
28° N
26° N

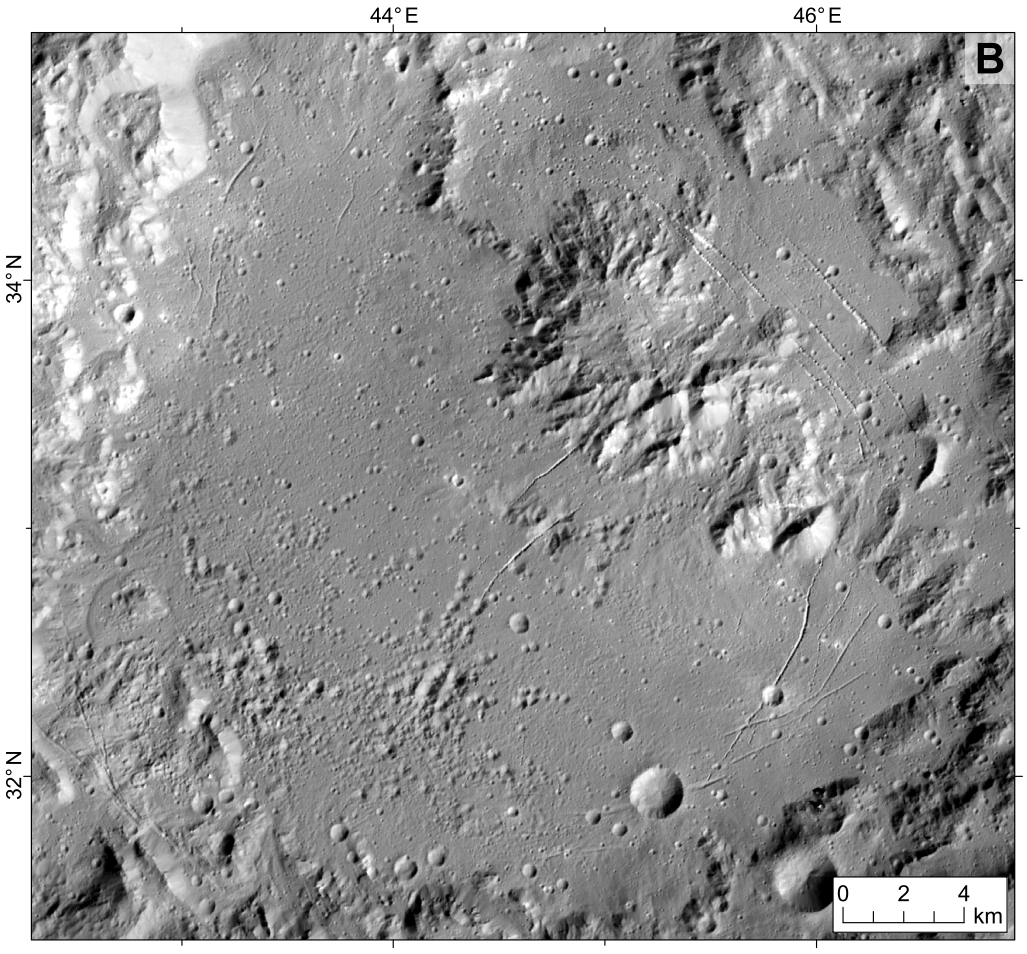
B
0 2 4 km
44° E
46° E
34° N
32° N

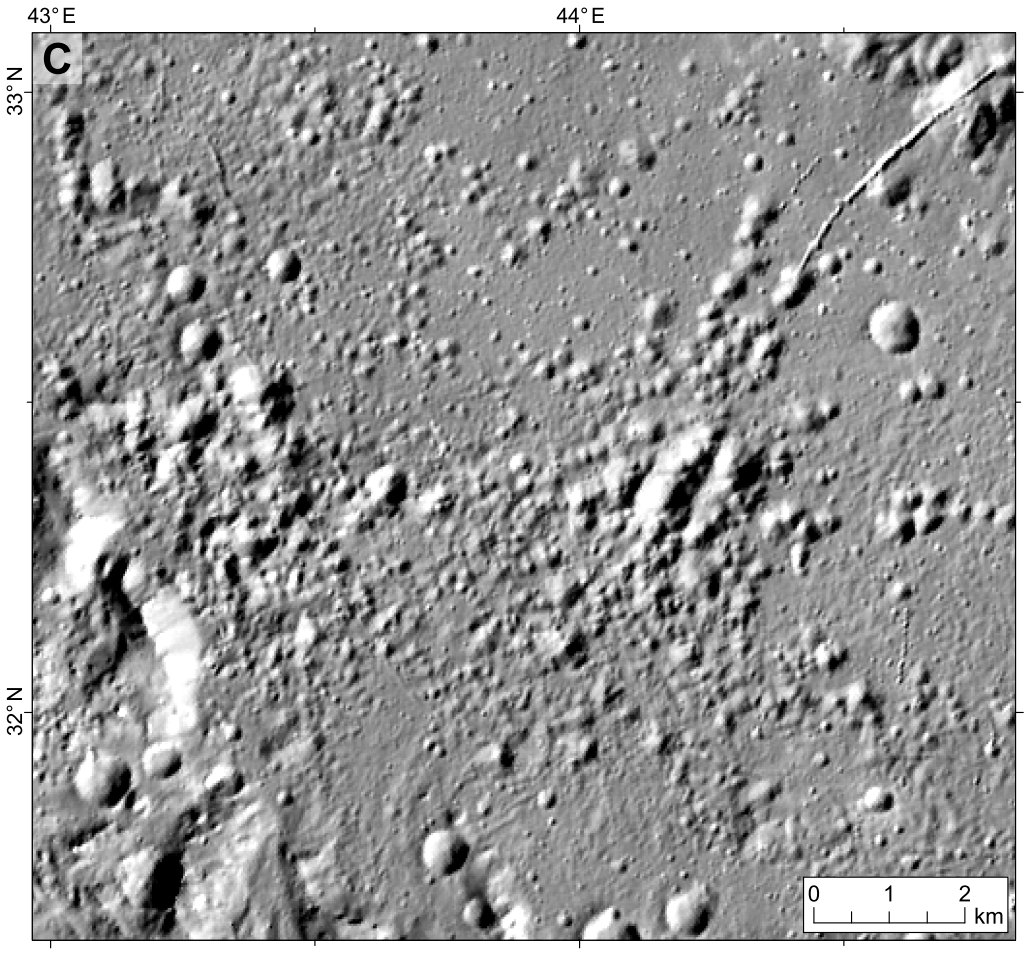
C
0 1 2 km
43° E
44° E
33° N
32° N

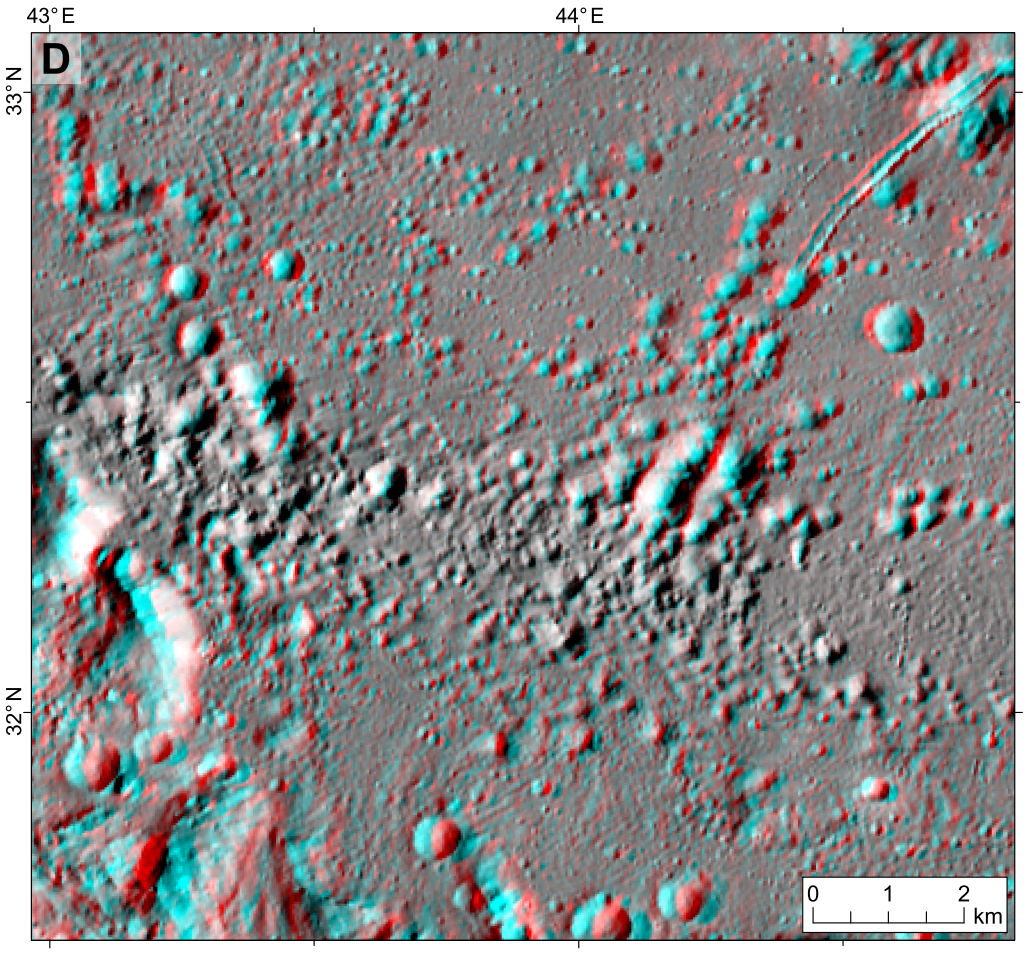
D
0 1 2 km
43° E
44° E
33° N
32° N

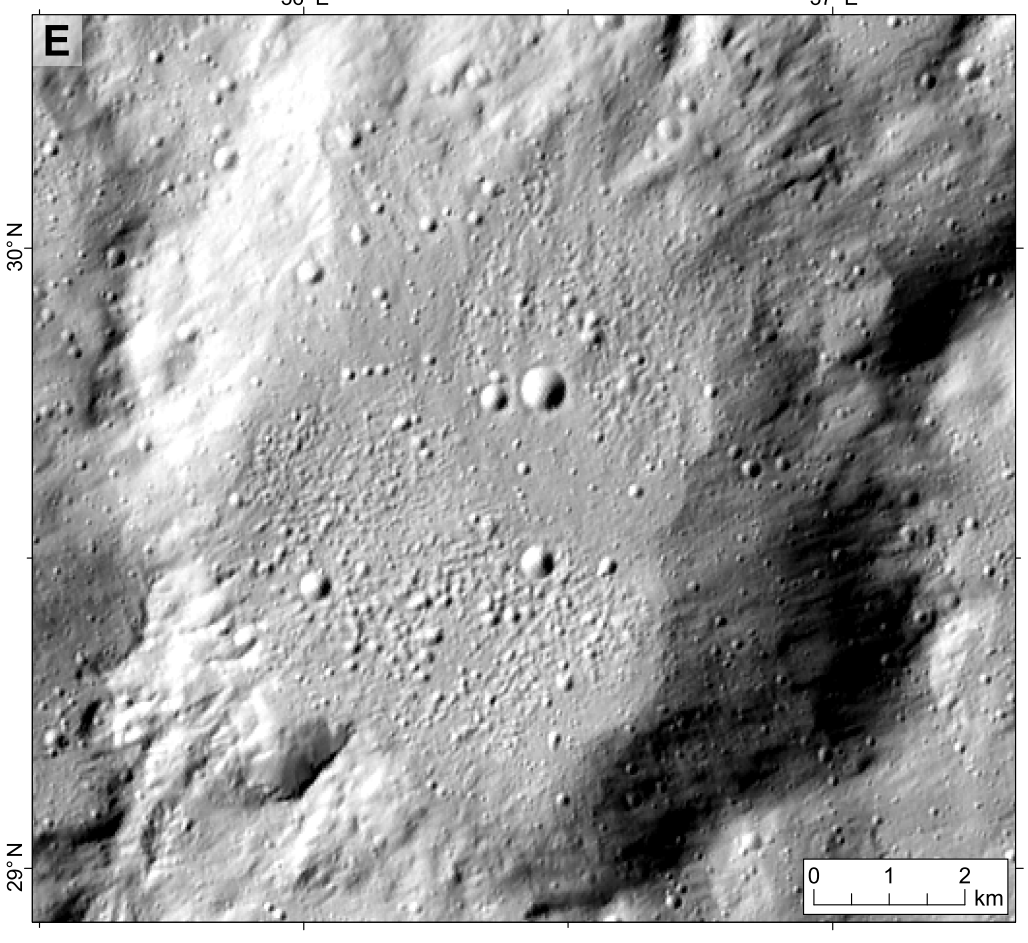
E
0 1 2 km
36° E
37° E
30° N
29° N

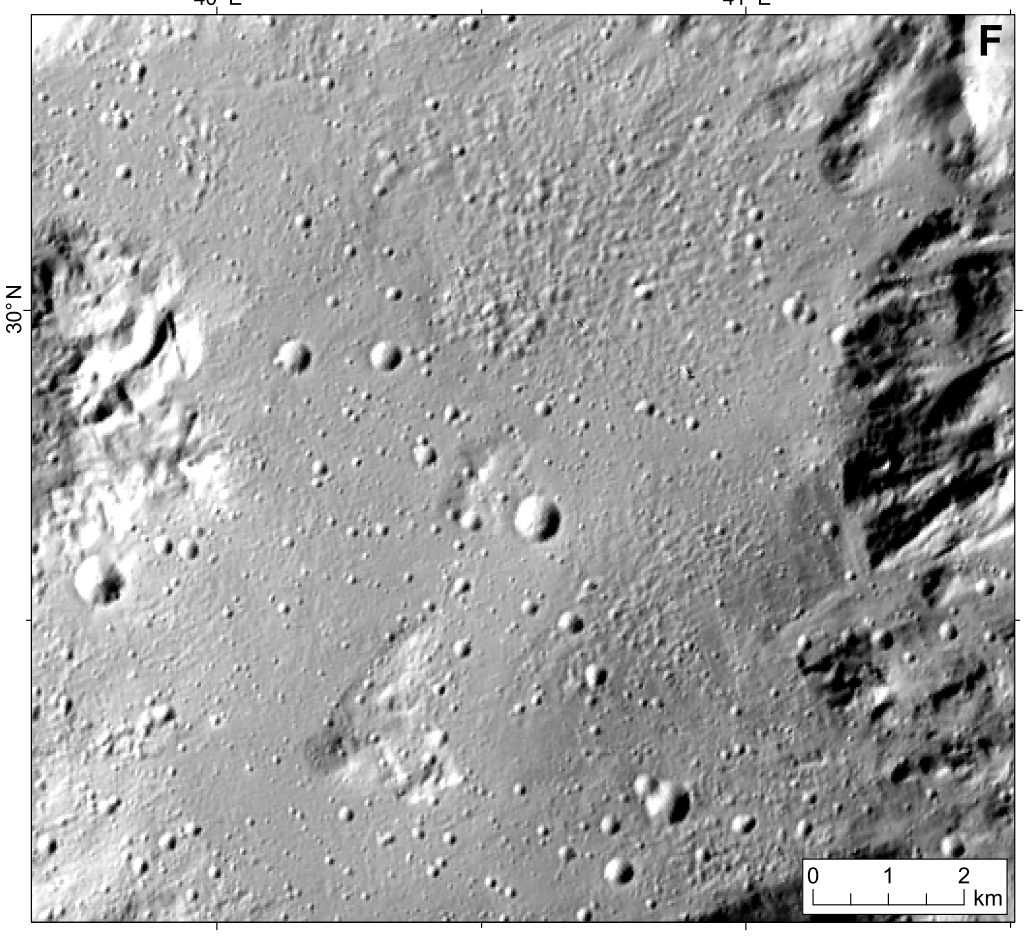
F
0 1 2 km
40° E
41° E
30° N

Fig. S1: Pitted terrain interior and exterior to Ikapati Crater (D=50km, 33.84°N/45.61°E).

(**A**) Broader surrounding terrain of Ikapati crater with superimposed HAMO stereophotogrammetry-based digital elevation model (≈137 m/px); colour-coded heights are given relative to the reference ellipsoid 482 km × 482 km × 446 km (Preusker et al., 2016). White boxes show the locations displayed in panels **C-D**. (**B**) Crater floor of Ikapati. (**C**) Pitted terrain in the southwestern portion of Ikapati's floor. (**D**) 3D anaglyph of panel **C** based on Framing Camera images 62,213 and 74,141. (**E**) Pitted terrain in an 10.9-km diameter, unnamed crater located southwest of Ikapati (see panel **A** for location). (**F**) Pitted terrain in an 16.8-km diameter, unnamed crater southwest of Ikapati (see panel **A** for location). All scenes except **D** are excerpts of the Framing Camera panchromatic nadir mosaic (30 m/px; equidistant cylindrical projection centred at 31.5°N/41.5°E).

Annex 2

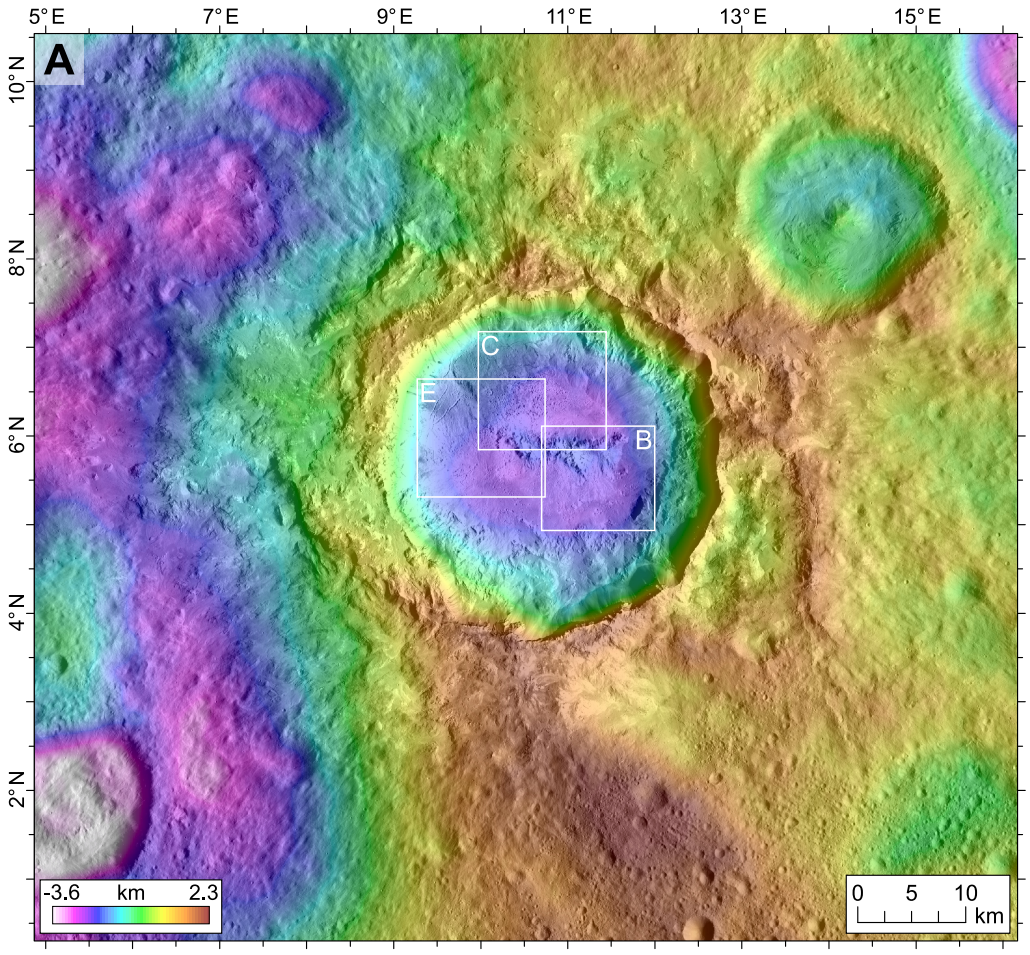
A
5° E
7° E
9° E
11° E
13° E
15° E
10° N
8° N
6° N
4° N
2° N
C
E
B
-3.6 km 2.3
0 5 10 km

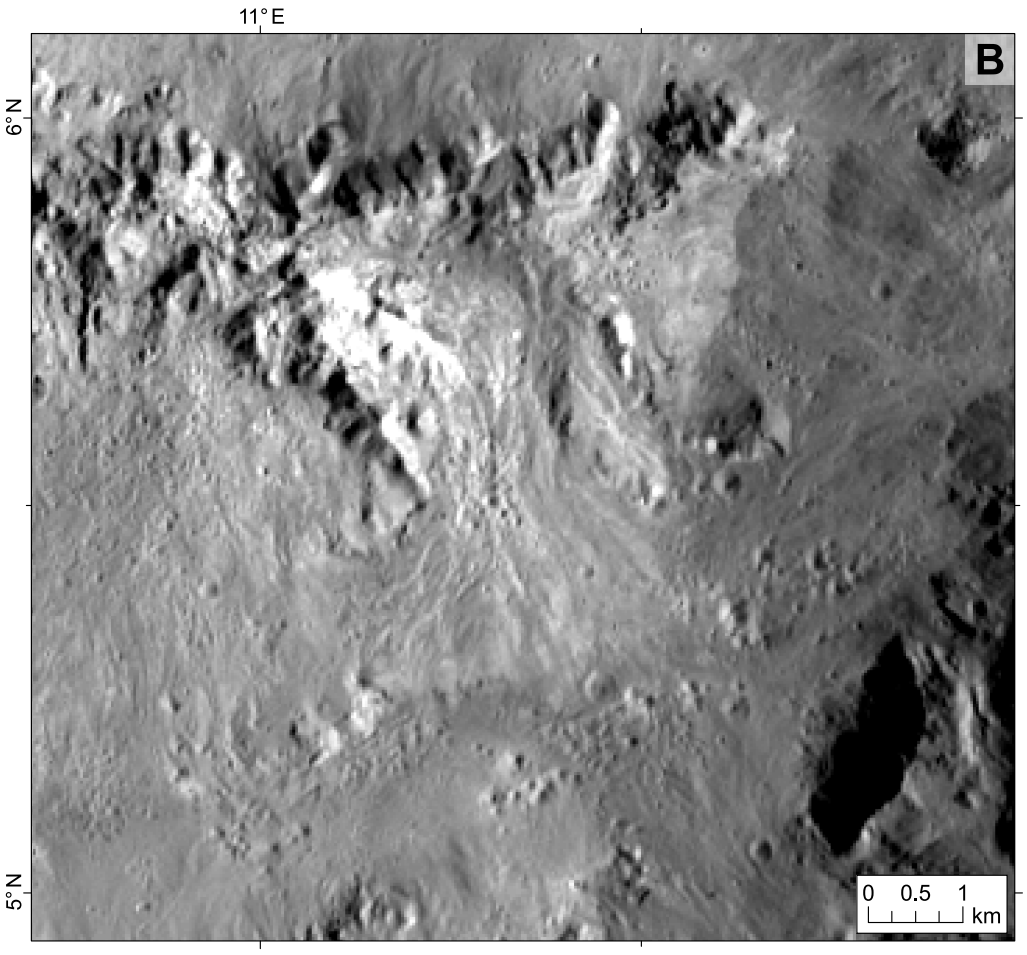
B
11° E
6° N
5° N
0 0.5 1 km

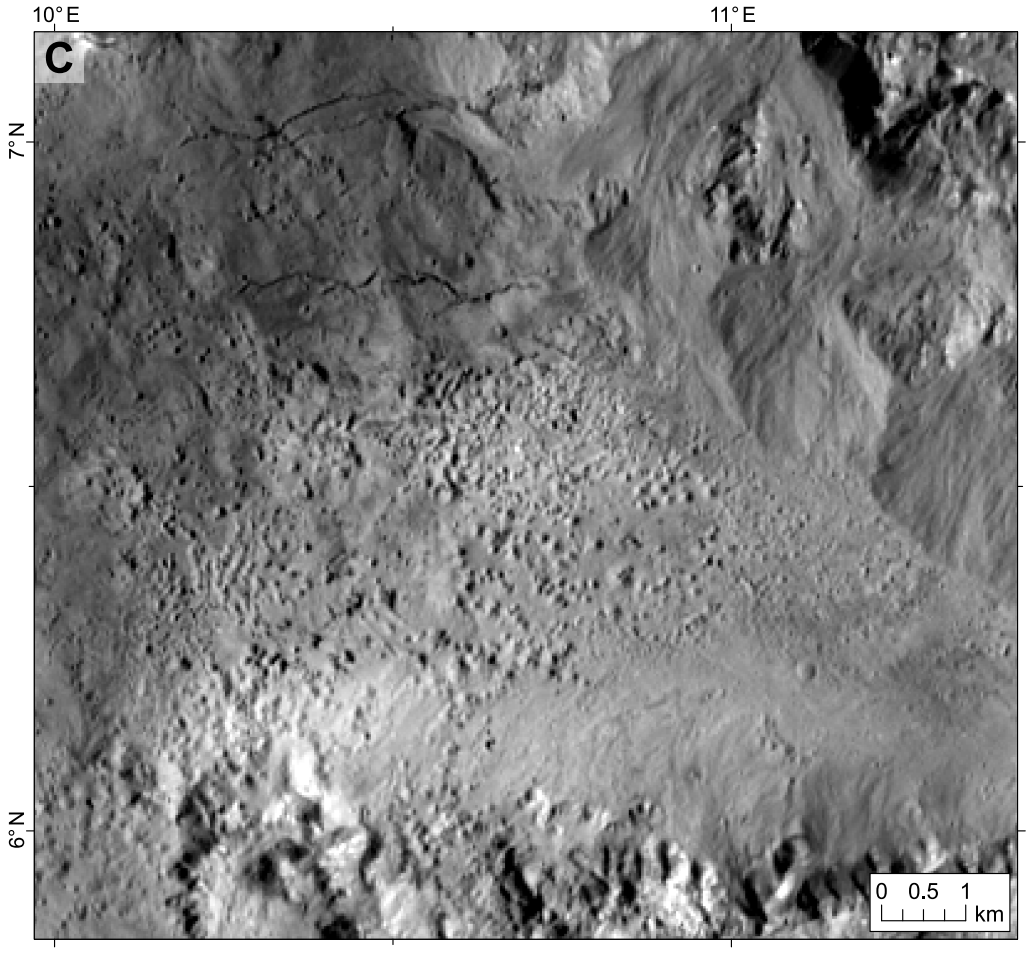
C
10° E
11° E
7° N
6° N
0 0.5 1 km

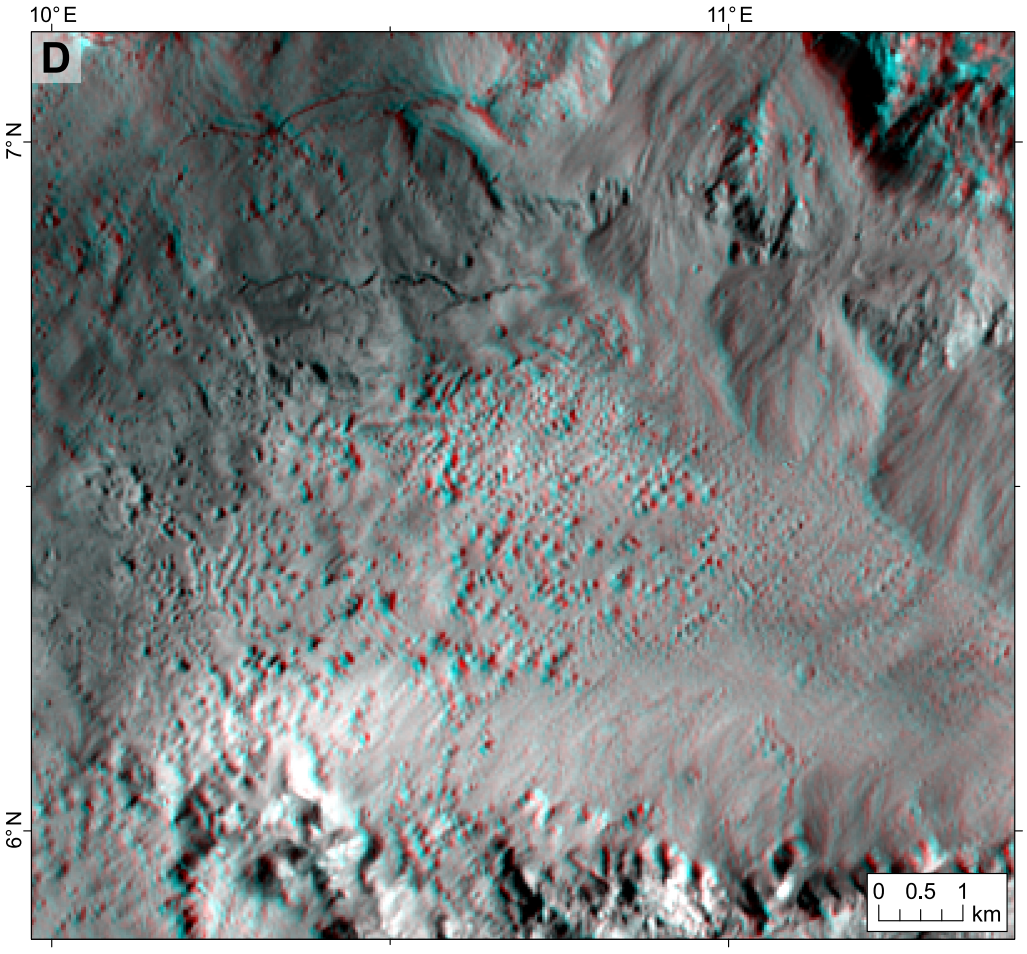
D
10° E
11° E
7° N
6° N
0 0.5 1 km

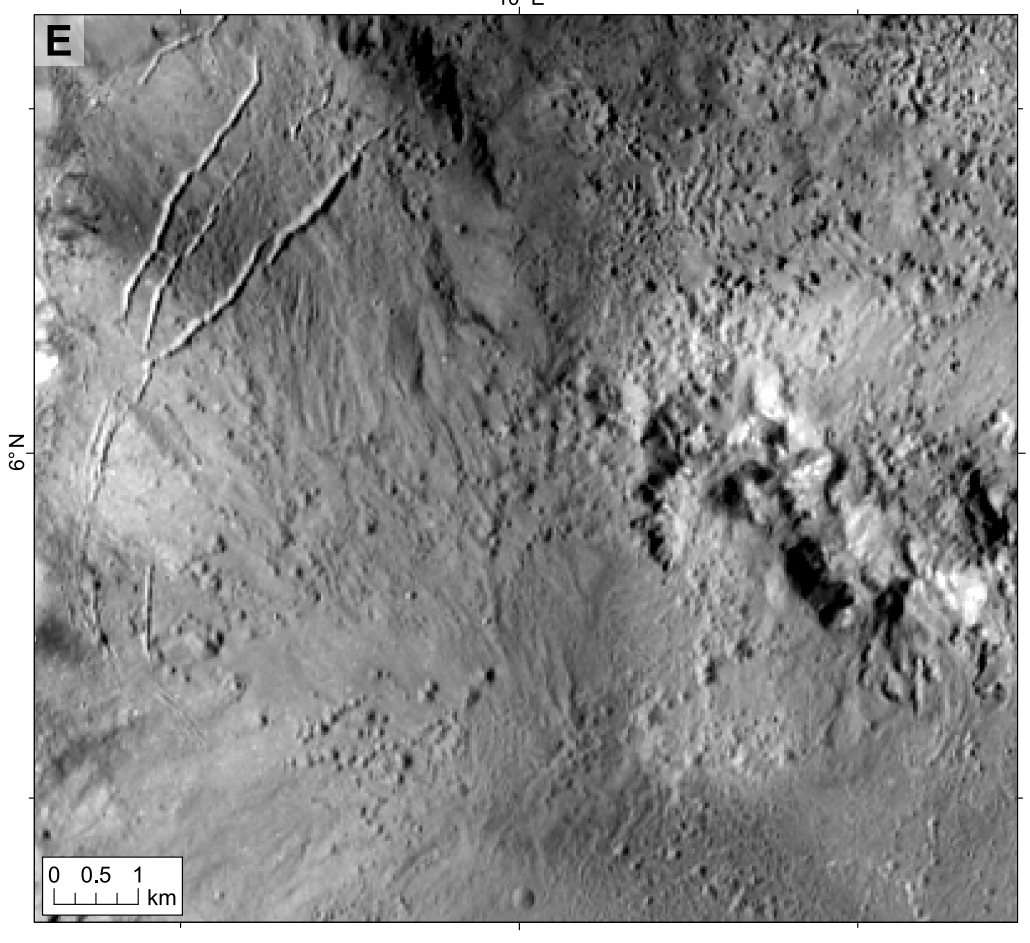
E
10° E
6° N
0 0.5 1 km

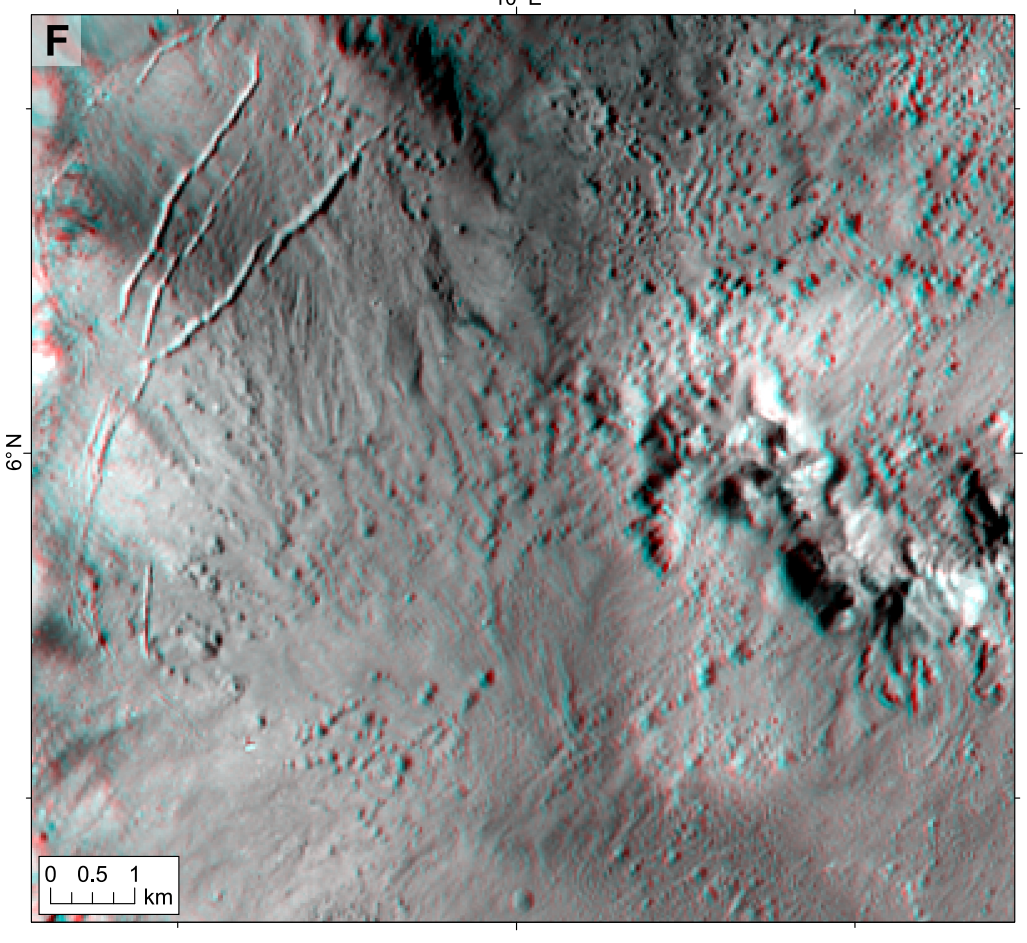
F
10° E
6° N
0 0.5 1 km

Fig. S2: Pitted terrain on the floor of Haulani Crater (D=34 km, 5.8°N/10.77°E).

(A) Overview of the broader region surrounding Haulani Crater with superimposed HAMO stereophotogrammetry-based digital elevation model (≈137 m/px); colour-coded heights are given relative to the reference ellipsoid 482 km × 482 km × 446 km (Preusker et al., 2016). White boxes show the locations displayed in panels **B-E**. (**B**) Pitted terrain located southeast of the central ridge. (**C**) Pitted terrain north of the central ridge developed within crater floor and talus materials. (**D**) 3D anaglyph of panel **C** based on Framing Camera images 62,828 and 54,293. (**E**) Pitted terrain west and southwest of the central ridge developed within crater floor and talus materials. (**F**) 3D anaglyph of panel **E** based on Framing Camera images 62,828 and 54,293. All scenes except **D** and **F** are excerpts of the Framing Camera panchromatic nadir mosaic (30 m/px; equidistant cylindrical projection centred at 5.8°N/10.8°E).

Annex 3

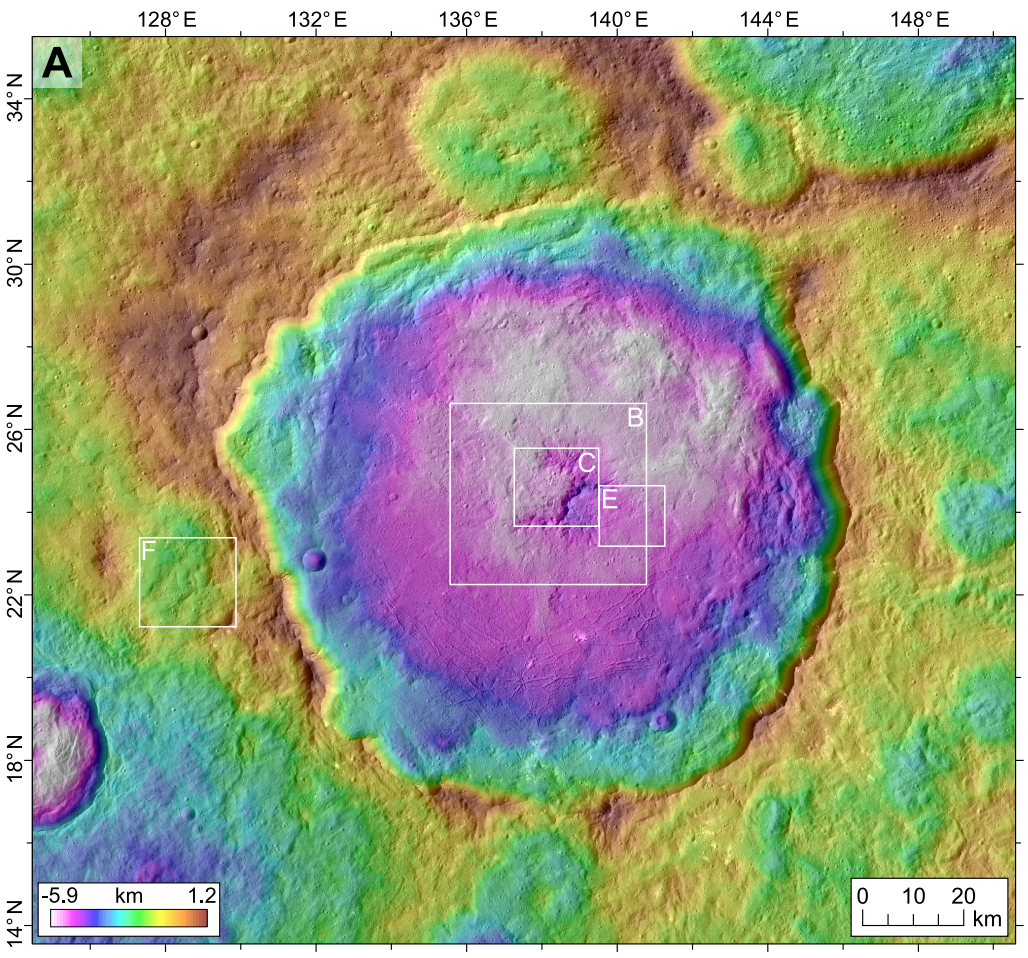
A
128° E
132° E
136° E
140° E
144° E
148° E
34° N
30° N
26° N
22° N
18° N
14° N
B
C
E
F
-5.9 km 1.2
0 10 20 km

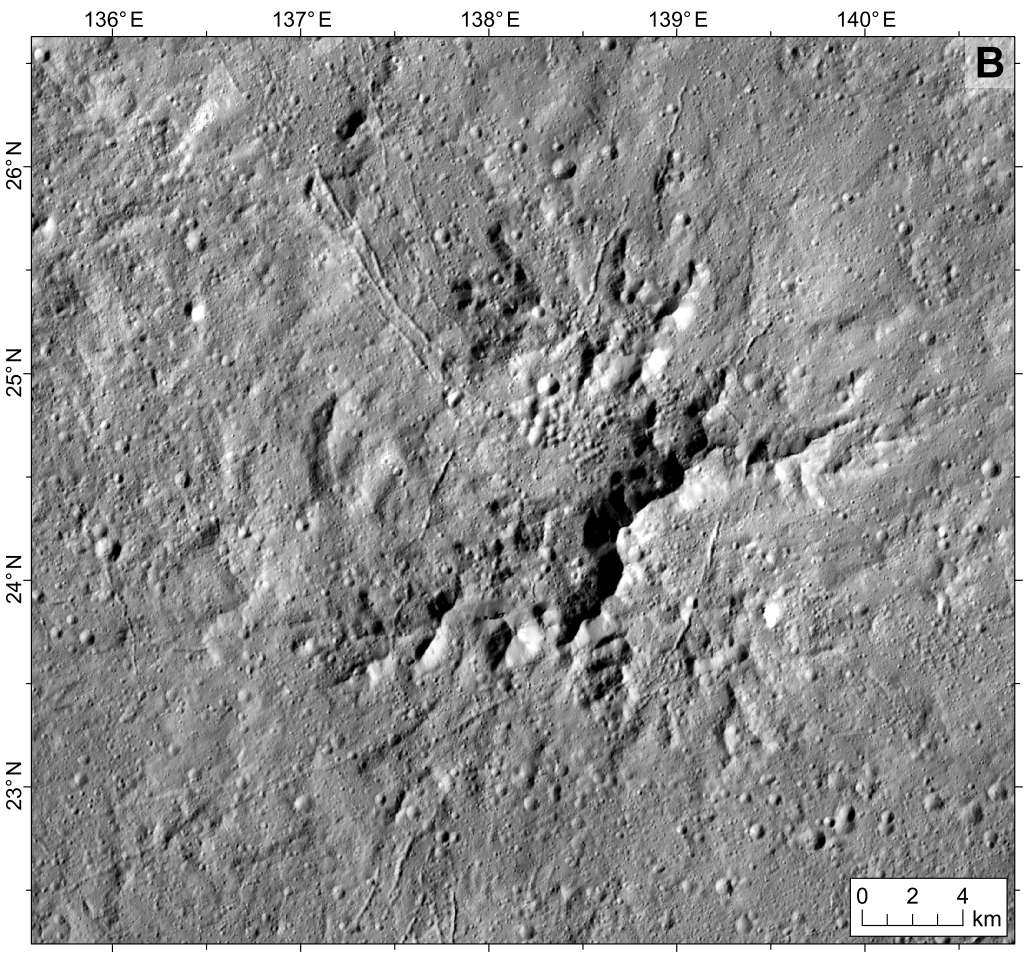
B
136° E
137° E
138° E
139° E
140° E
26° N
25° N
24° N
23° N
0 2 4 km

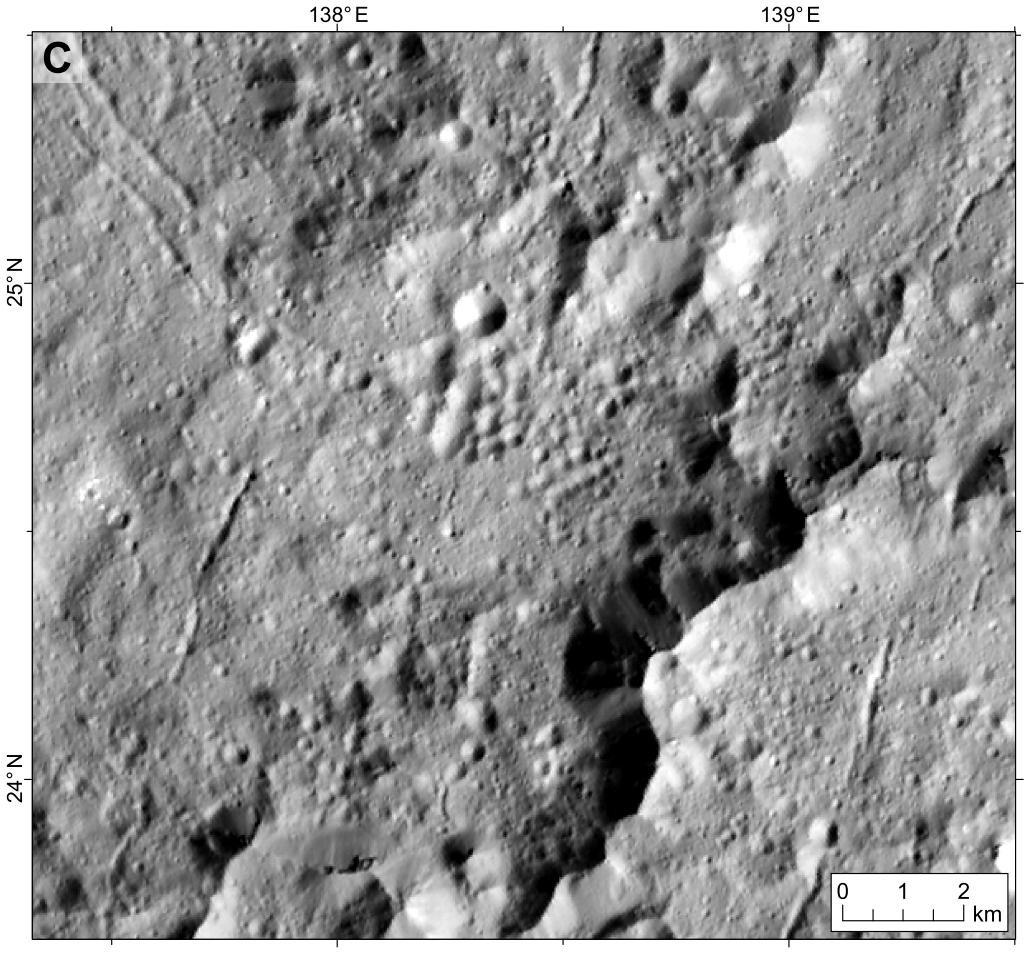
C
138° E
139° E
25° N
24° N
0 1 2 km

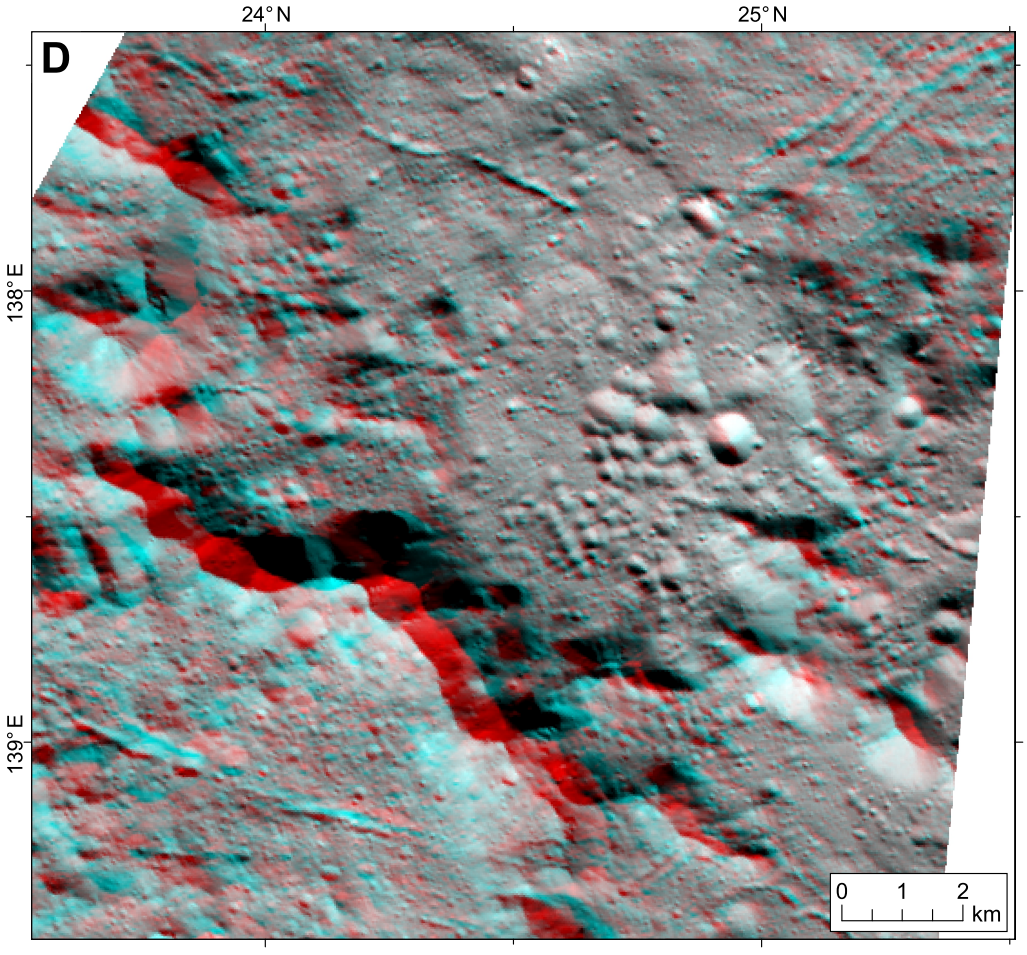
D
24° N
25° N
138° E
139° E
0 1 2 km

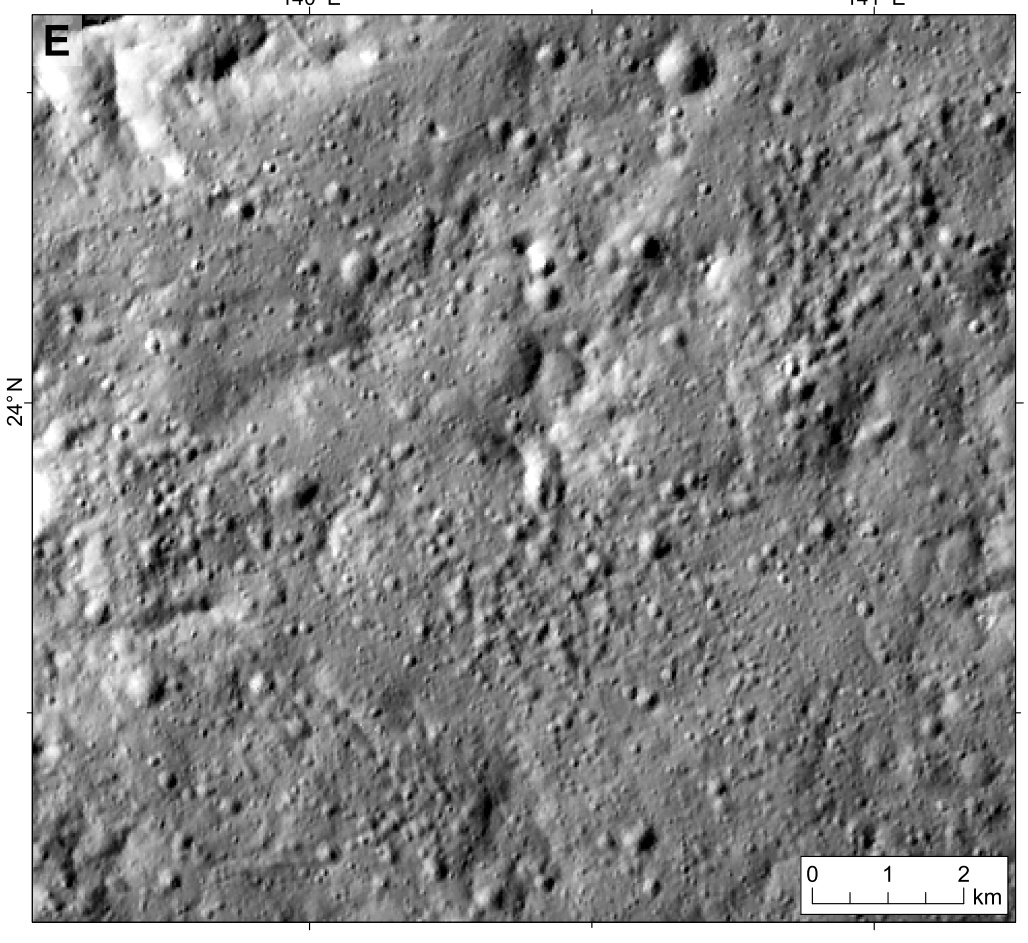
E
140° E
141° E
24° N
0 1 2 km

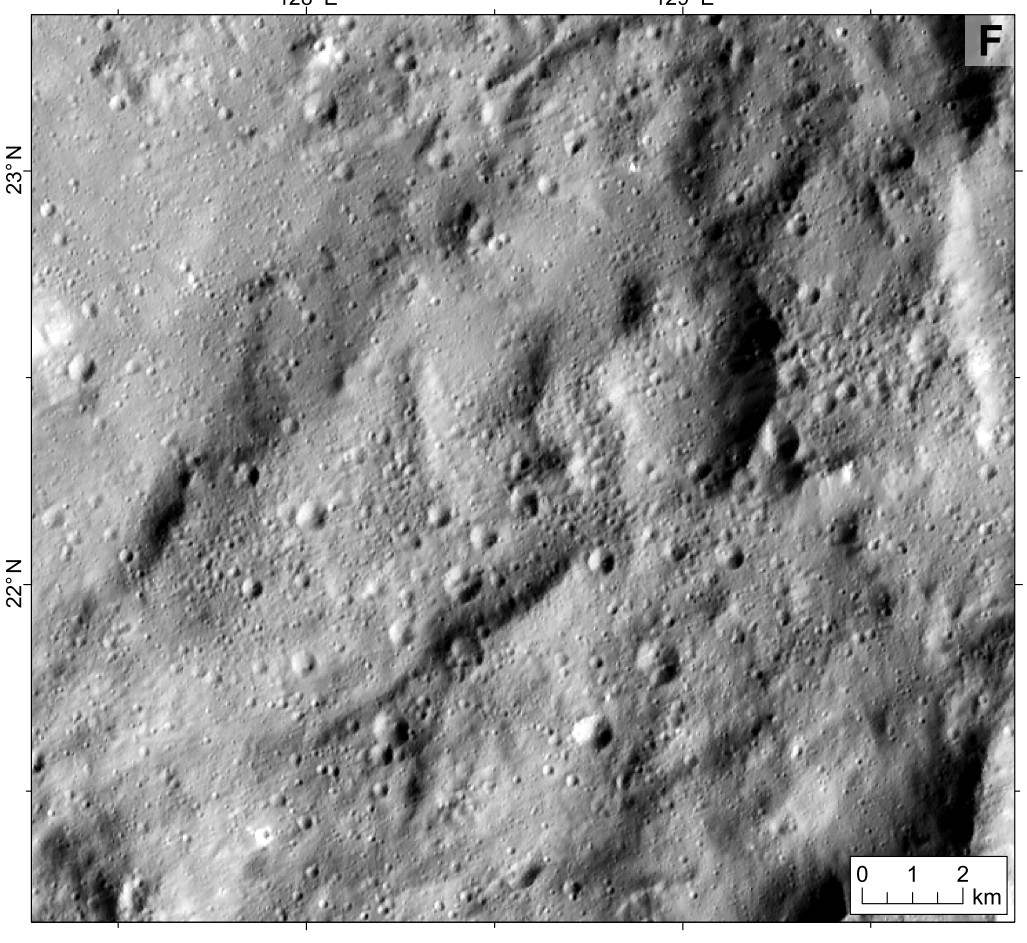
F
128° E
129° E
23° N
22° N
0 1 2 km

Fig. S3: Pitted terrain interior and exterior to Dantu Crater (D=126 km, 24.3°N/138.23°E).

(A) Overview of Dantu and its immediate surrounding terrain with superimposed HAMO stereophotogrammetry-based digital elevation model (≈137 m/px); colour-coded heights are given relative to the reference ellipsoid 482 km × 482 km × 446 km (Preusker et al., 2016). White boxes show the locations displayed in panels **B**-**F**. (**B**) Overview of Dantu's central peak complex. (**C**) Close-up of the central peak with pitted terrain developed in an area which may resemble a collapsed central pit. (**D**) 3D anaglyph of panel **C** based on Framing Camera images 72,706 and 72952. Note north is to the right. (**E**) Pitted terrain east to southeast of the central peak developed within crater floor material. (**F**) Pitted terrain developed within rim material. All scenes except **D** are excerpts of the Framing Camera panchromatic nadir mosaic (30 m/px; equidistant cylindrical projection centred at 24.5°N/137.5°E).

Annex 4

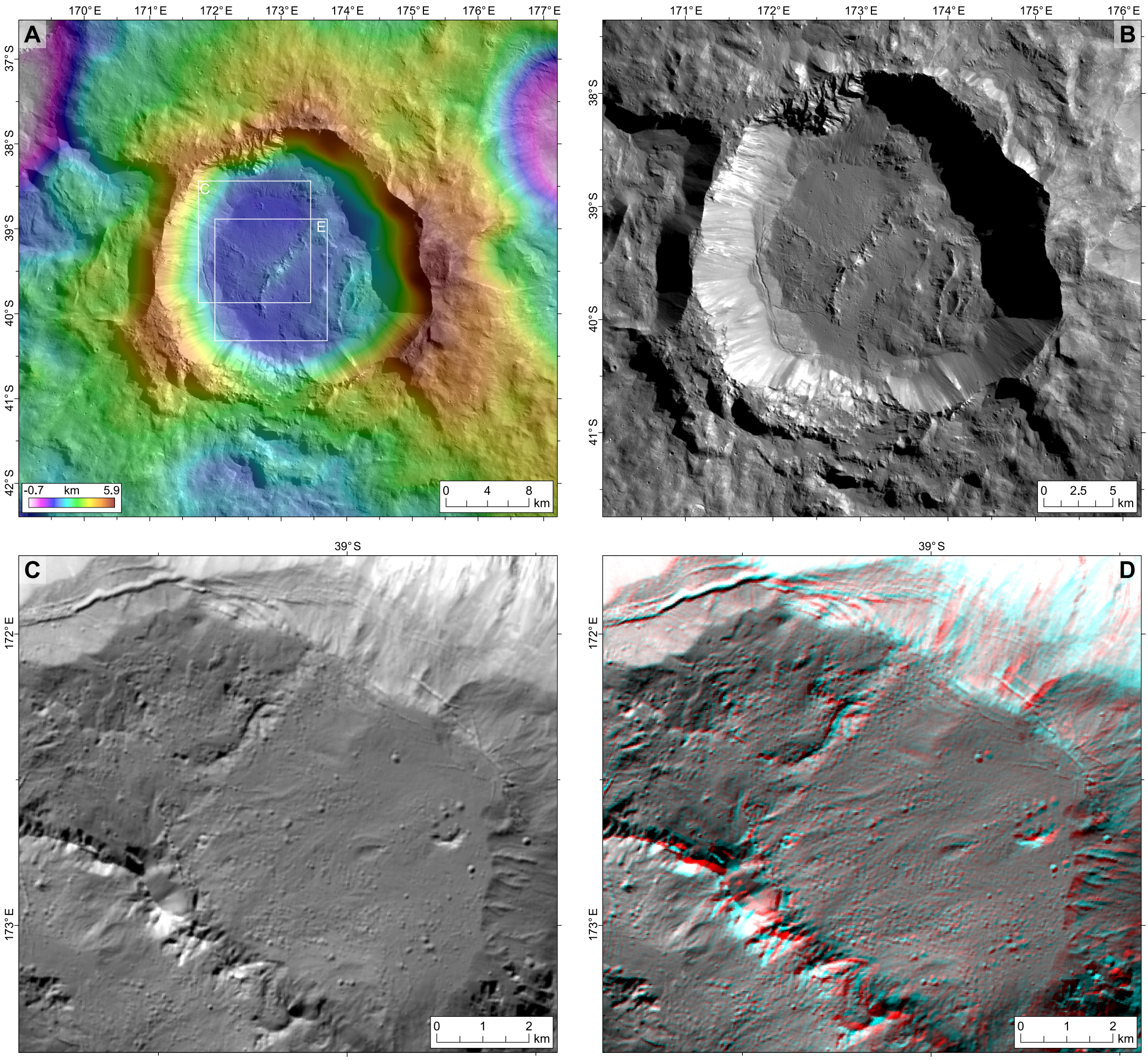
A
170° E
171° E
172° E
173° E
174° E
175° E
176° E
177° E
37° S
38° S
39° S
40° S
41° S
42° S
C
E
-0.7 km 5.9
0 4 8 km
B
171° E
172° E
173° E
174° E
175° E
176° E
38° S
39° S
40° S
41° S
0 2.5 5 km
C
39° S
172° E
173° E
0 1 2 km
D
39° S
172° E
173° E
0 1 2 km
E
40° S
39° S
173° E
0 1 2 km
F
40° S
39° S
173° E
0 1 2 km

Fig. S4: Pitted terrain on the floor of Kupalo Crater (D=26 km, -39.44°N/173.2°E).

(**A**) Overview of Kupalo and its vicinity with superimposed HAMO stereophotogrammetry-based digital elevation model (≈137 m/px); colour-coded heights are given relative to the reference ellipsoid 482 km × 482 km × 446 km (Preusker et al., 2016). White boxes show the locations displayed in panels **C**-**F**. (**B**) Kupalo as viewed in panchromatic imagery. (**C**) Pitted terrain northwest of the central ridge developed in crater floor material. (**D**) 3D anaglyph of panel **C** based on Framing Camera images 72,529 and 73,137. (**E**) Pitted terrain southeast of the central ridge developed in crater floor material. (**F**) 3D anaglyph of panel **E** based on Framing Camera images 72,529 and 73,137. All scenes except **D** and **F** are excerpts of the Framing Camera panchromatic nadir mosaic (30 m/px; equidistant cylindrical projection centred at 24.5°N/137.5°E). Note north is not up in panels **C**-**F**.

Annex 5

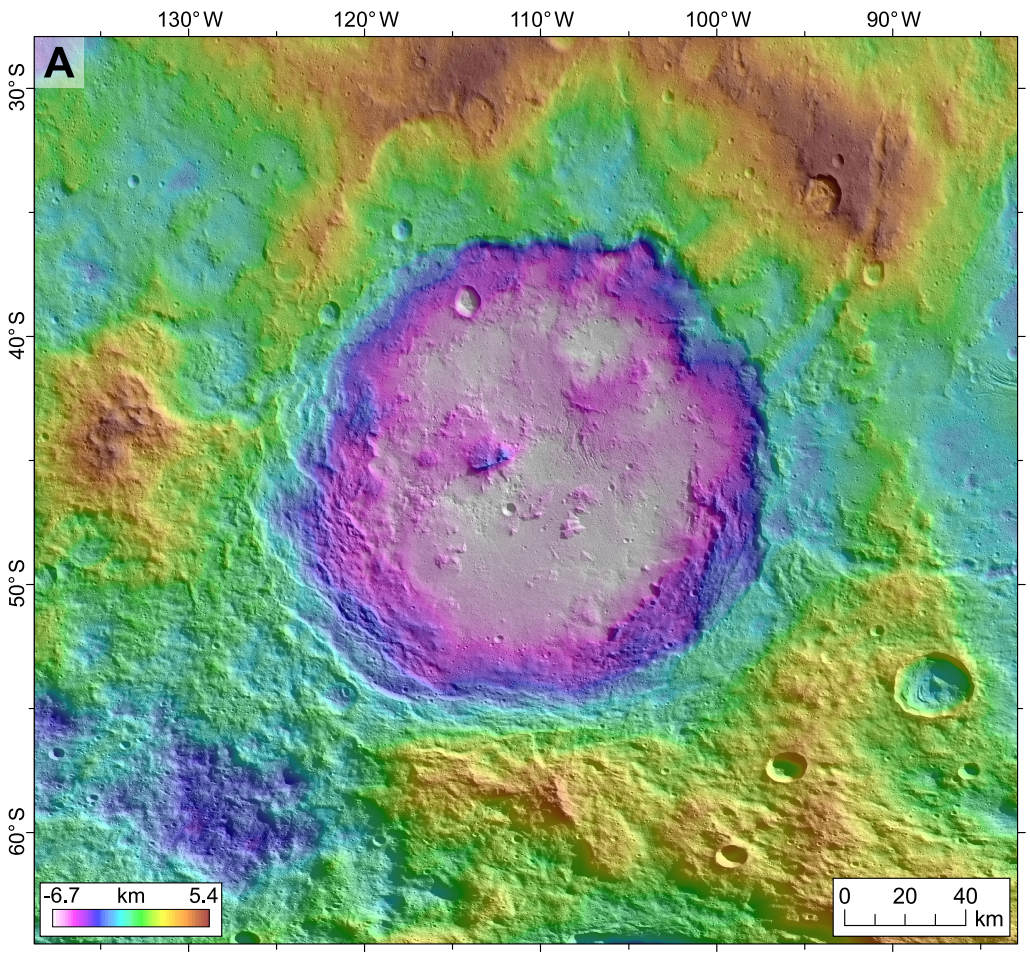
A
130° W
120° W
110° W
100° W
90° W
30° S
40° S
50° S
60° S
-6.7 km 5.4
0 20 40 km

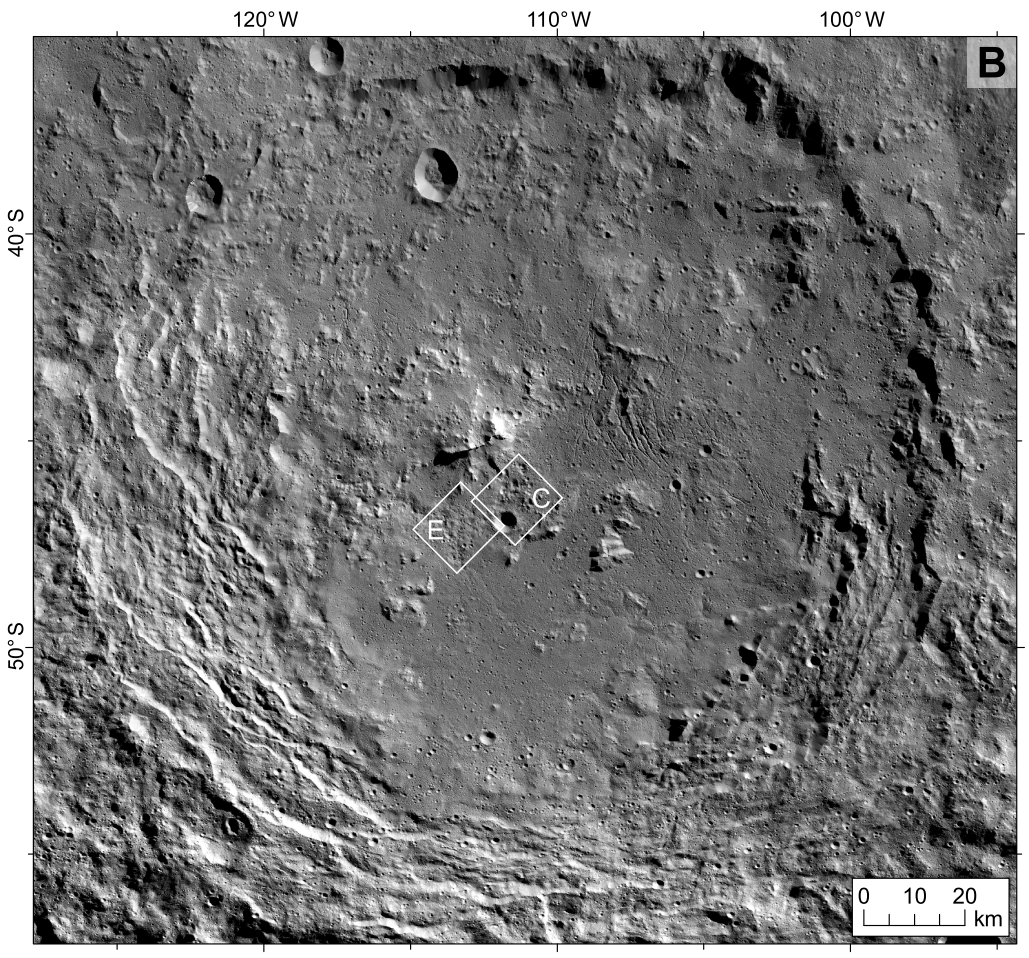
B
120° W
110° W
100° W
40° S
50° S
E
C
0 10 20 km

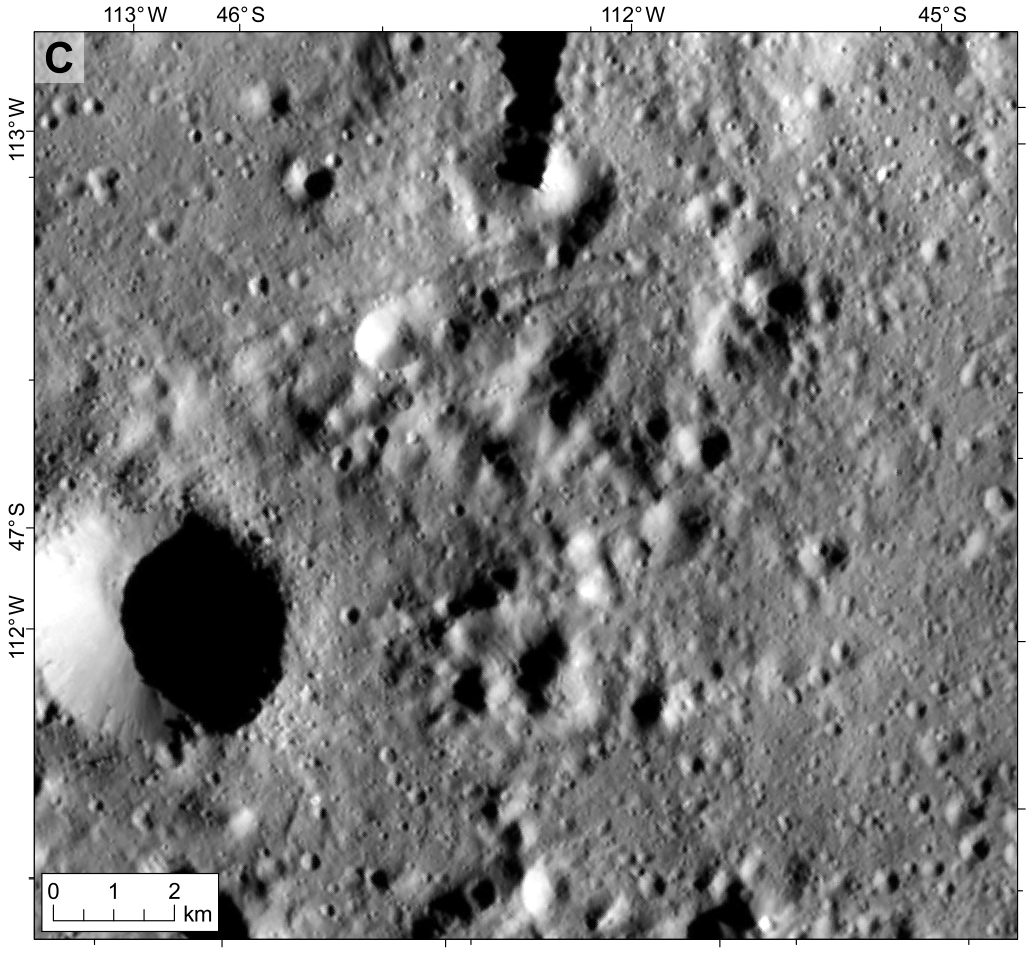
C
113° W
46° S
112° W
45° S
113° W
47° S
112° W
0 1 2 km

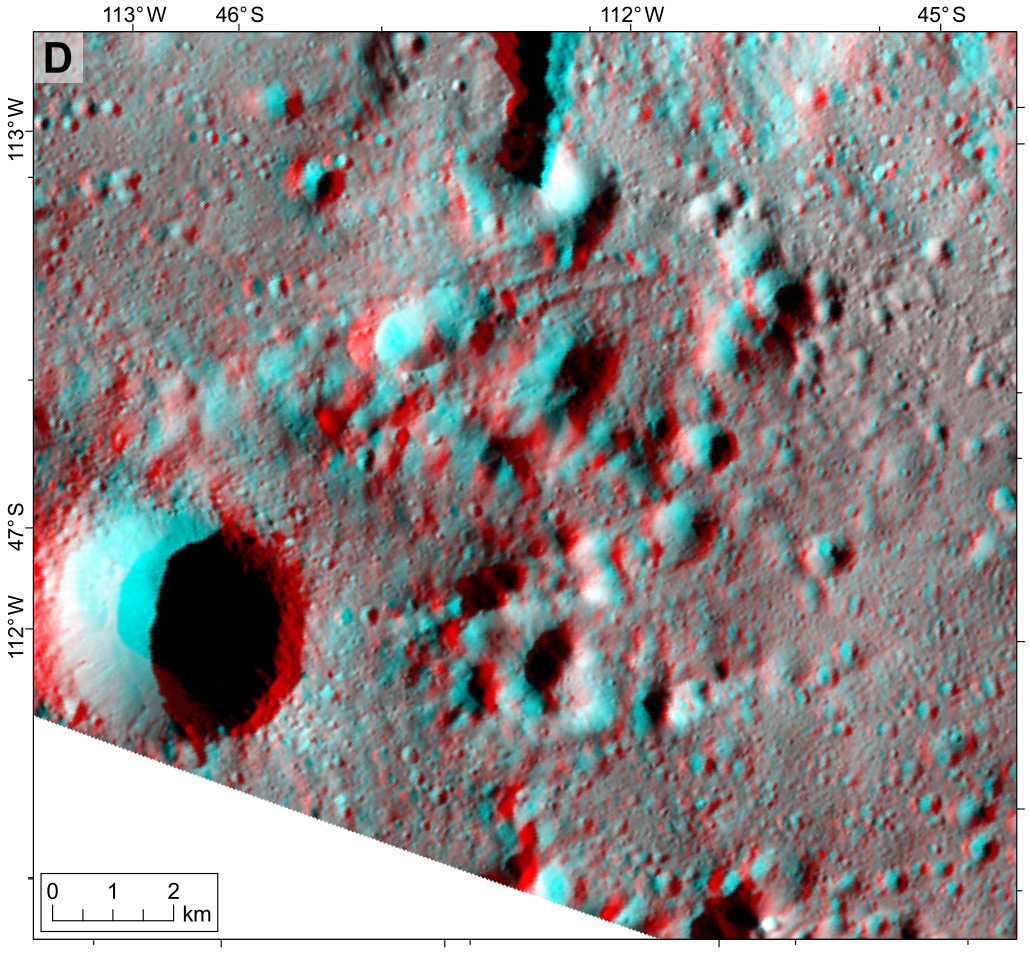
D
113° W
46° S
112° W
45° S
113° W
47° S
112° W
0 1 2 km

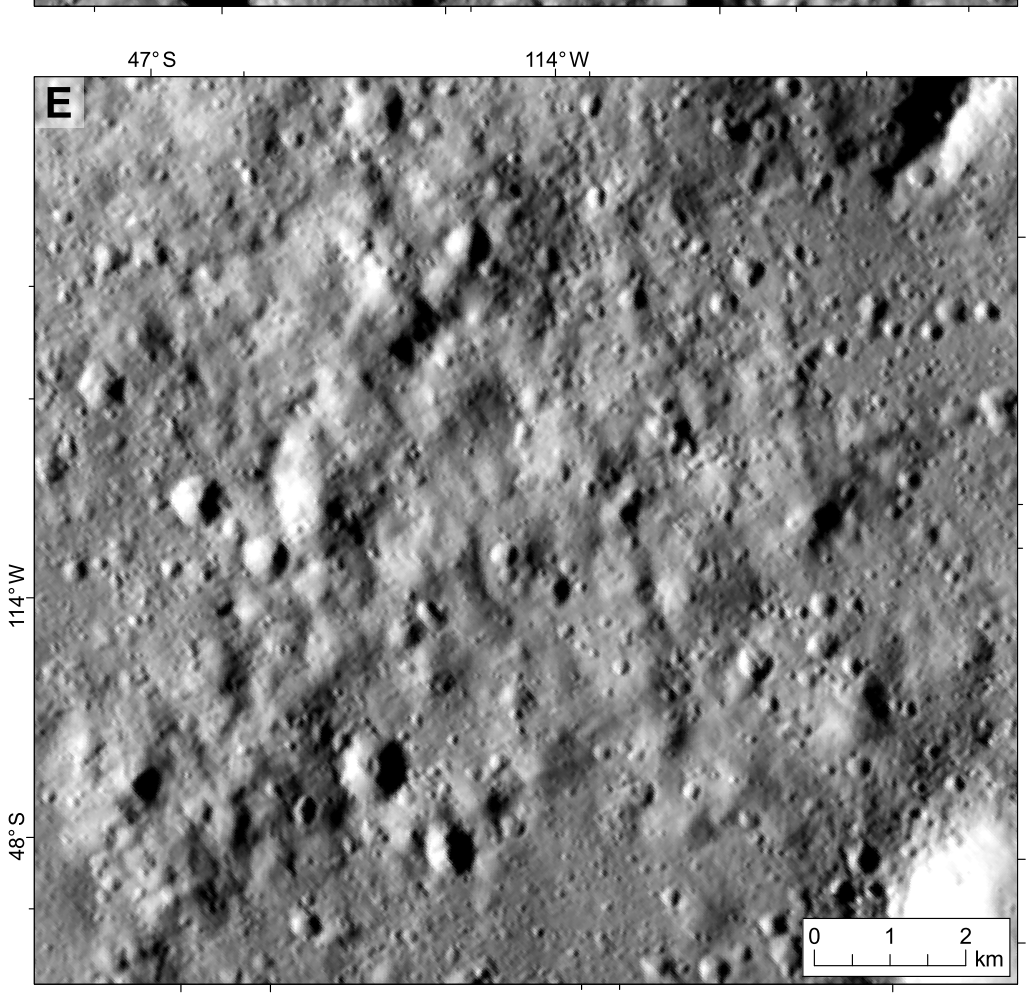
E
47° S
114° W
114° W
48° S
0 1 2 km

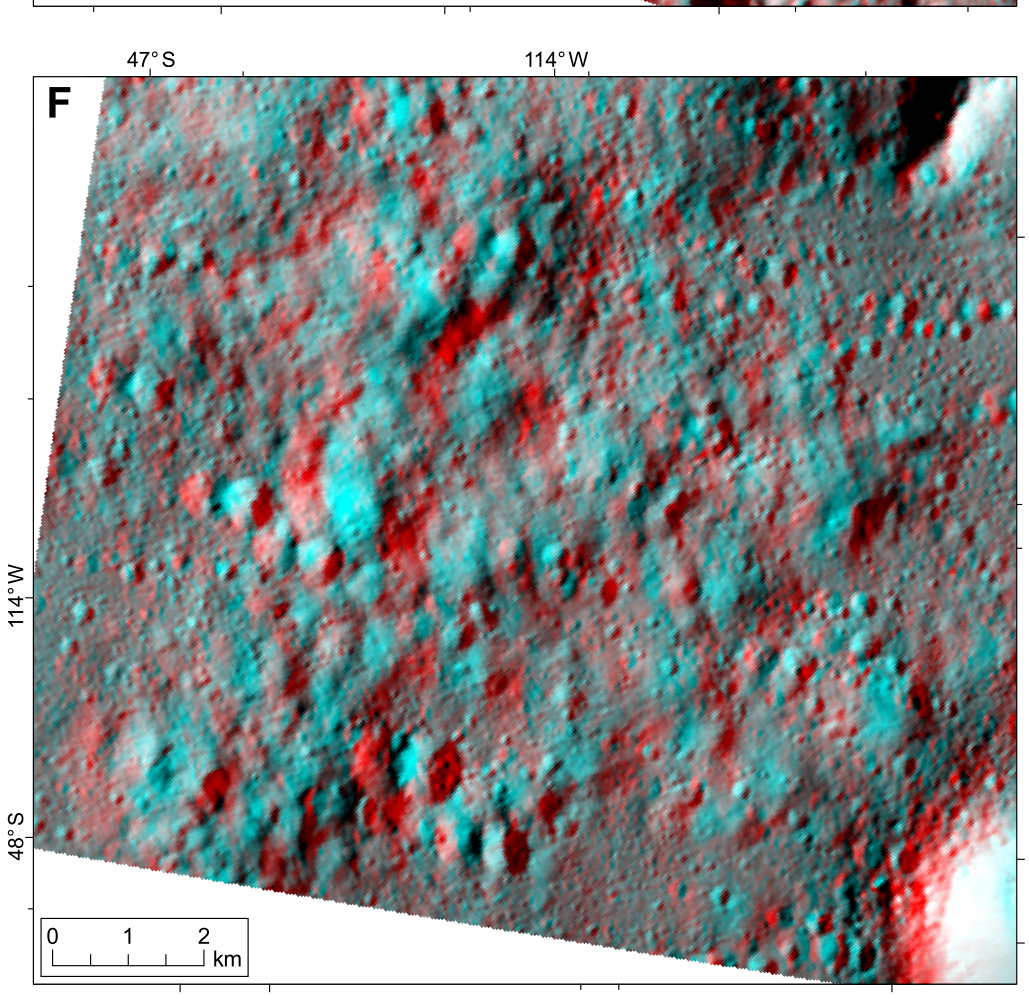
F
47° S
114° W
114° W
48° S
0 1 2 km

Fig. S5: Degraded pitted terrain in close proximity of the central peak of Uravara Crater (D=170 km, -45.66°N/249.24°E).

(**A**) Overview of broader region surrounding the Urvara basin with superimposed HAMO stereophotogrammetry-based digital elevation model (≈137 m/px); colour-coded heights are given relative to the reference ellipsoid 482 km × 482 km × 446 km (Preusker et al., 2016). (**B**) Urvara basin with white boxes showing the locations displayed in panels **C-F**. (**C**) Potential pitted terrain southeast of the central peak developed within crater floor materials. (**D**) 3D anaglyph of panel **C** based on Framing Camera images 76,696 and 63,512. (**E**) Potential pitted terrain south of the central peak developed within crater floor materials. (**F**) 3D anaglyph of panel **E** based on Framing Camera images 80,342 and 55,129. All scenes except **D** and **F** are excerpts of the Framing Camera panchromatic nadir mosaic (30 m/px; equidistant cylindrical projection centred at -44.8°N/ 248.9°E). Note north is not up in panels **C-F**.

References:

Becker, K. J., R. W. Gaskell, L. LeCorre, V. Reddy 2015. Hayabusa and Dawn Image Control from Generation of Digital Elevation Models for Mapping and Analysis. *46th Lunar and Planetary Science Conference*, abstract #2955.

Blewett et al. 2011. Hollows on Mercury: MESSENGER Evidence for Geologically Recent Volatile-Related Activity. *Science*, 333, 1856-1859.

Boyce, J. M., L. Wilson, P. J. Mouginis-Mark, C. W. Hamilton, L. L. Tornabene 2012. Origin of small pits in martian impact craters. *Icarus, 221,* 262-275.

Byrne, S. and Ingersoll, A. P. 2003. A Sublimation Model for Martian South Polar Ice Features. *Science*, 299, 1051-1053.

Capria, M. T., F. Tosi, M. C. De Sanctis, F. Capaccioni, E. Ammannito, A. Friegeri, F. Zambon, S. Fonte, E. Palomba, D. Turrini, T. N. Titus, S. E. Schröder, M. Toplis, J.-Y. Li, J.-P. Combe, C. A. Raymond, C. T. Russell 2014. Vesta surface thermal properties map. *Geophys. Res. Let.,* doi: 10.1002/2013GL059026.

Denevi, B. W., D. T. Blewett, D. L. Buczkowski, F. Capaccioni, M. T. Capria, M. C. de Sanctis, W. B. Garry, R. W. Gaskell, L. Le Corre, J.-Y. Li, S. Marchi, T. J. McCoy, A. Nathues, D. P. O'Brien, N. E. Petro, C. M. Pieters, F. Preusker, C. A. Raymond, V. Reddy, C. T. Russell, P. Schenk, J. E. C. Scully, J. M. Sunshine, F. Tosi, D. A. Williams, D. Wyrick 2012. Pitted terrain on Vesta and implications for the presence of volatiles. *Science, 338*, 246-249.

Kneissl, T., S. van Gasselt, G. Neukum 2011. Map-projection-independent crater size-frequency determination in GIS environments – New software tool for ArcGIS. *Planetary and Space Science, 59,* 1243-1254.

Malin, M. C. and K. S. Edget 2001. Mars Global Surveryor Mars Orbiter Camera: Interplanetary cruse through primary mission. *J. Geophys. Res. – Planets, 110,* 23429-23570.

Malin, M. C., Caplinger, M. A., and Davis, S. D. 2001. Observational Evidence for an Active Surface Reservoir of Solid Carbon Dioxide on Mars. *Science*, 294, 2146-2148.

Marchi et al. 2013. High-velocity collisions from the lunar cataclysm recorded in asteroidal meteorites. *Nature Geoscience*, 6, 303-307.

Mouginis-Mark, P. J., and H. Garbiel 2007. Crater geometry and ejecta thickness of the martian impact crater Tooting. *Meteorit. Planet. Scie. 42,* 1615-1625.

Preblich, B., A. McEwen, D. Studer 2007. Mapping rays and secondary craters from Zunil, Mars. *J. Geophys. Res. – Planets, 112,* doi:10.1029/2006JE002817.

Preusker, F., et al. 2016. Dawn at Ceres – Shape Model and Rotational State. *47th Lunar and Planetary Science Conference*, abstract #1954.

Reddy, V., et al. 2012. Color and albedo heterogeneity of Vesta from Dawn. *Science 336,* doi: 10.1126/science.1219088.

Rivkin, A. S. et al. 2010. The Surface Composition of Ceres. *Space Science Reviews 163*, 95-116.

Schorghofer, N. 2008. The lifetime of ice on main belt asteroids. *Ap. J., 682,* 697-705.

Schorghofer, N. 2016. Predictions of depth-to-ice on asteroids based on an asynchronous model of temperature, impact stirring, and ice loss. *Icarus 276*, 88- 95.

Tosi, F., M. T. Capria, M. C. De Sanctis, J.-Ph. Combe, F. Zambon, A. Nathures, S. E. Schröder, J.-Y. Li, E. Palomba, A. Longbardo, D. T. Blewett, B. W. Denevi, E. Palmer, F. Capaccioni, E. Ammanito, T. M. Titus, D. W. Mittlefehldt, J. M. Sunshine, C. T. Russell, C. A. Raymond 2014. Thermal measurements of dark and bright surface features on Vesta as derived from Dawn/VIR. *Icarus, 240,* 36-57.

Tornabene, L. L., et al. 2006. Indentification of large (2-10 km) rayed craters on Mars in THEMIS thermal infrared images: Implications for possible martian meteorite source rgeions. *J. GEophys. Res. – Planets, 111.* Doi:10.1029/2005JE002600.

Tornabene, L. L., et al. 2012. Widespread crater-related pitted materials on Mars: Further evidence for the role of target volatiles during the impact process. *Icarus, 220,* 348-368.